CRS-stack-based seismic imaging workflow—a real data example

Z. Heilmann, J. Mann, E. Duveneck, and T. Hertweck

email: *Zeno.Heilmann@gpi.uni-karlsruhe.de*

keywords: *CRS stack, kinematic wavefield attributes, tomographic inversion, depth migration*

ABSTRACT

In recent years, it has been demonstrated by many case studies that the Common-Reflection-Surface (CRS) stack produces reliable stack sections with high resolution and superior signal-to-noise ratio compared to conventional methods. In contrast to such conventional methods like the common-midpoint stack or the sequence normal-moveout correction/dip-moveout correction/stack, an entire set of physically interpretable stacking parameters is determined as a by-product of the data-driven stacking process. These kinematic wavefield attributes obtained by the CRS stack may be even more important than the stacked section itself because they can be applied to solve a number of dynamic and kinematic stacking, modeling, and inversion problems. CRS-stack-based seismic imaging makes use of these extended possibilities in further processing. Here, we present a real data example demonstrating the basic steps of this data-driven imaging approach, namely the CRS stack, the determination of a smooth macrovelocity model via CRS-attribute-based tomographic inversion, and, finally, pre- and/or poststack depth migration. As is shown, not only the poststack but also the prestack depth migration benefits from this approach. Additional CRS-stack-based processing steps that may be applied in the future of the ongoing project are, e. g., residual static corrections using CRS stacking operators, limited-aperture migration based on the estimated projected Fresnel zone, determination of the geometrical spreading factor, and amplitude-variation-with-offset analysis in the time domain using approximate common-reflection-point trajectories calculated from CRS attributes.

INTRODUCTION

The datasets used for this case study were acquired in the close vicinity of Karlsruhe, Germany, during summer 2003 by *Deutsche Montan Technologie GmbH* (DMT), Essen, Germany. The acquisition was performed for *HotRock EWK Offenbach/Pfalz GmbH* (HotRock), Karlsruhe, Germany, with the intention to obtain a structural image of the investigated subsurface relevant for of a projected geothermal power plant near Karlsruhe. The power plant shall be based on two boreholes, one for production and one for re-injection of thermal water. The boreholes are planed to be drilled in 2004 to a depth of ≈ 2.5 km, where a strongly fractured horizon of hot-water-saturated lacustrine limestone is located. As the achievable production rate depends mainly on the degree of fracturing of the target horizon and the number of faults reached by the boreholes, a detailed knowledge of the subsurface structure is essential. For this reason, two almost parallel seismic lines with a separation of ≈ 2.5 km and a length of ≈ 12 km each were acquired.

DMT applied a standard preprocessing and imaging sequence to the datasets, the latter consisting of normal-moveout (NMO) correction/dip-moveout (DMO) correction/stack, finite-differences (FD) time migration, and a time-to-depth conversion using macrovelocity models based on stacking velocity sections. As an alternative to this standard processing, the main steps of the CRS-stack-based seismic imaging workflow were carried out in the framework of a research cooperation between HotRock, DMT, and Karlsruhe University. Additional steps such as residual static corrections using CRS stacking operators (Koglin and Ewig, 2002), true-amplitude migration, and amplitude-variation-with-offset (AVO) analysis may follow in the course of the further collaboration.

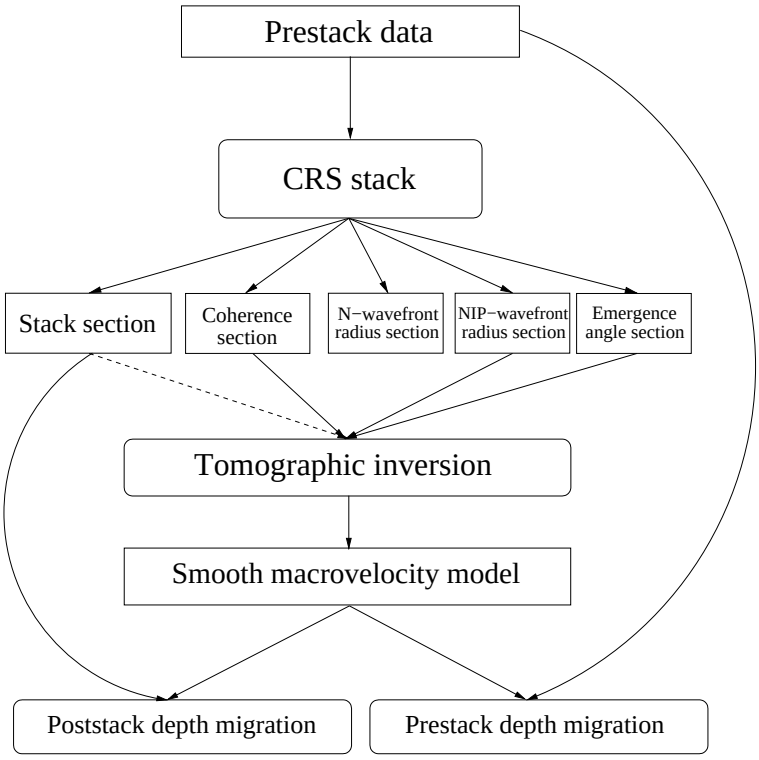

Figure 1: The CRS-stack-based seismic imaging workflow.

APPLICATION OF A CRS-STACK-BASED SEISMIC IMAGING WORKFLOW

Starting point for the CRS-stack-based seismic imaging workflow (Figure 1) was the preprocessed multi-coverage seismic reflection data provided by DMT. The preprocessing was performed in different steps of filtering, amplitude correction, muting, deconvolution, field static correction, and residual static correction.

CRS stack

Within the course of this project, the CRS stack method (see, e. g., Müller, 1998; Jäger, 1999; Mann, 2002) was complemented by a smoothing algorithm which is applied to the obtained CRS attributes in an event-consistent way (Mann and Duveneck, 2003, in this report) in order to use them for the final optimization and stacking iteration. This approach led to a significant enhancement of event continuity and consistency with the underlying theory for both seismic lines. The final stack was restricted to the projected first Fresnel zone calculated from the obtained CRS attributes. The simulated zero-offset (ZO) sections are displayed in Figures 2 and 3. The respective coherence sections indicating the fit between the determined CRS stacking operators and the reflection events in the prestack data are shown in Figures 4 and 5.

As can be seen, the overall image quality is quite high. Below the particularly strong reflector at $\approx 1.5\,\mathrm{s}$ the number of detected events decreases abruptly. This reflector was identified as the upper edge of the so-called *Pechelbronner Schichten*, an alternating stratification of siltstone, claystone, and sandstone. For traveltimes $< 1.5\,\mathrm{s}$, some regions with little coherent energy can be observed. These regions coincide with the locations of faults and fractures complicating the wavefield such that only little coherent energy can be found along the hyperbolic CRS stacking operator.

The comparison between the CRS results and the results obtained by the above-mentioned standard processing reveals a generally higher image quality of the former, especially with respect to signal-to-noise ratio and reflector continuity. In particular, for traveltimes $> 1.5\,\mathrm{s}$, the main target area below the *Pechelbronner Schichten*, the CRS stack resolves events that are not visible in the NMO/DMO/stack results.

As indicated in Figure 1, the CRS stack procedure provides, in addition to the stack and coherence sections, three different sections of kinematic wavefield attributes (CRS attributes). These are:

- a section containing the emergence angle of the ZO (or normal) ray (Figures 6 and 7) with respect to the measurement-surface normal.
- a section containing the radius of the normal-incidence-point (NIP) wavefront (Figures 8 and 9) as observed at the emergence point of the normal ray. The NIP wave focuses at that point of the reflector, where the respective normal ray is reflected, i. e., at the NIP.
- a section containing the curvature of the normal wavefront (Figures 10 and 11) which would be observed at the emergence point of the normal ray due to an exploding reflector element at the NIP.

The coherence sections depicted in Figures 4 and 5 were used in Figures 6-13 to mask out locations with very low coherence value because such locations are not expected to be associated with reliable attributes. From the emergence angle and NIP wave radius sections, optimized high-resolution stacking velocity sections have been calculated. These sections, displayed in Figures 12 and 13, can be used as input to conventional Dix-type inversions and for comparison with stacking velocities derived by means of NMO/DMO/stack.

Tomographic inversion

In order to obtain a depth image from the time-domain pre- and/or poststack data, a kinematically correct macrovelocity model needs to be constructed. Such a model can be obtained directly from the CRS stack results by means of a tomographic inversion method based on the kinematic wavefront attributes associated with the NIP wave (Duveneck, 2002). As depicted in Figure 1, these attributes are the radius of curvature of the NIP wavefront and the emergence angle of the normal ray. For the description of the smooth macrovelocity model two-dimensional B-splines are used by this method.

In this case study, about 1000 ZO samples together with the associated attribute values were picked for each profile to achieve an appropriate resolution and reliability. To reduce the effort involved in manual picking, the existing software was extended by a module performing automatic picking based on the coherence associated with the ZO samples. The picked data was checked using several criteria, in order to discriminate outliers and attributes related to multiples, before the tomographic inversion process was applied. The obtained macrovelocity models are displayed in Figures 14 and 15. Each of them is defined by 336 B-spline knots. All in all, the velocity models of Profiles A and B are very similar. However, considering the small distance between the two seismic lines, the minor differences between the two models reveal a strong lateral inhomogeneity of the investigated subsurface.

Prestack depth migration

Based on the macrovelocity models obtained in the previous step, we applied a Kirchhoff depth migration (Hertweck and Jäger, 2002; Jäger and Hertweck, 2002) to the prestack data of both profiles. For this, the necessary kinematic Green's function tables (GFTs) were calculated by means of an eikonal solver. The resulting depth-migrated prestack data was firstly muted to avoid excessive pulse stretch for shallow reflectors and then stacked in offset direction in order to obtain the depth-migrated images displayed in Figures 16 and 17. Both sections show a multitude of faults and fractures, which are clearly imaged even at larger depths. We compared these results to the results obtained in the course of the standard processing, where a finite difference time migration was applied after the NMO/DMO/stack process and the resulting time migrated images have been converted to the depth domain using stacking-velocity-based macrovelocity models. The results obtained by CRS-stack-based imaging show a higher resolution, especially in the target area, and the depth location of the reflectors was assessed to be more reliable. For comparison, the last step of the standard processing—the time-to-depth conversion—was repeated using the CRS-attribute-derived macrovelocity models. The results obtained this way are in good agreement with the results of the CRS-stack-based imaging workflow even though the overall resolution is lower. The comparison of our results with existing borehole data and other geological and geophysical information available for the investigated area shows a good agreement, too.

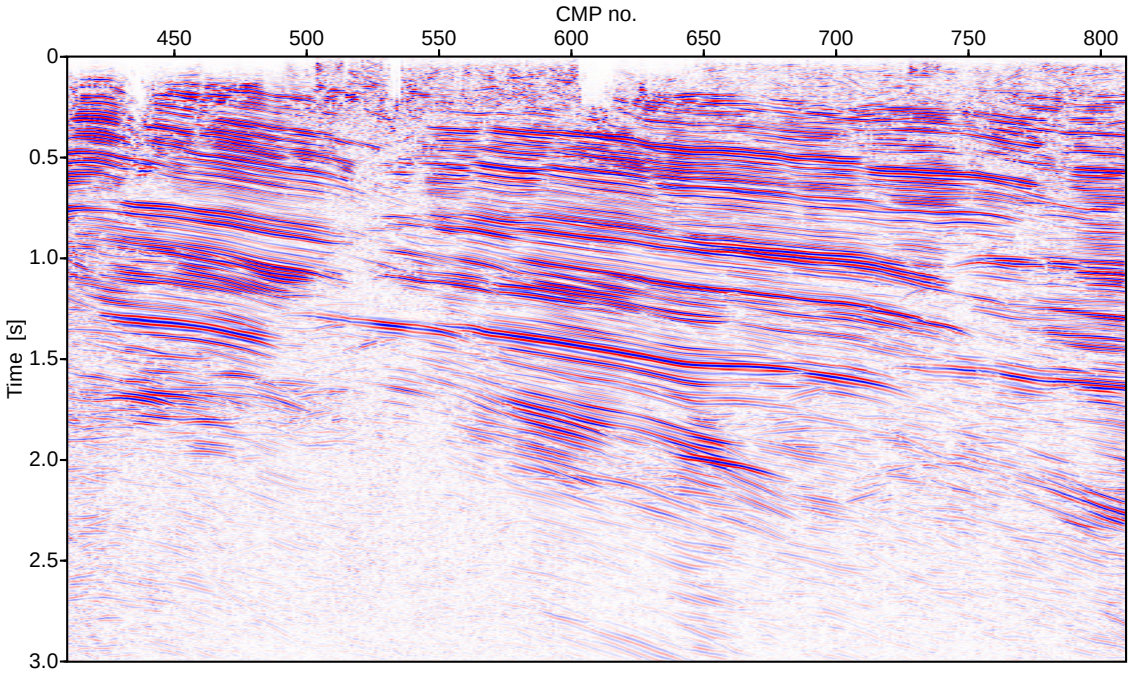

Figure 2: Result of the optimized CRS stack in the projected first Fresnel zone, Profile A.

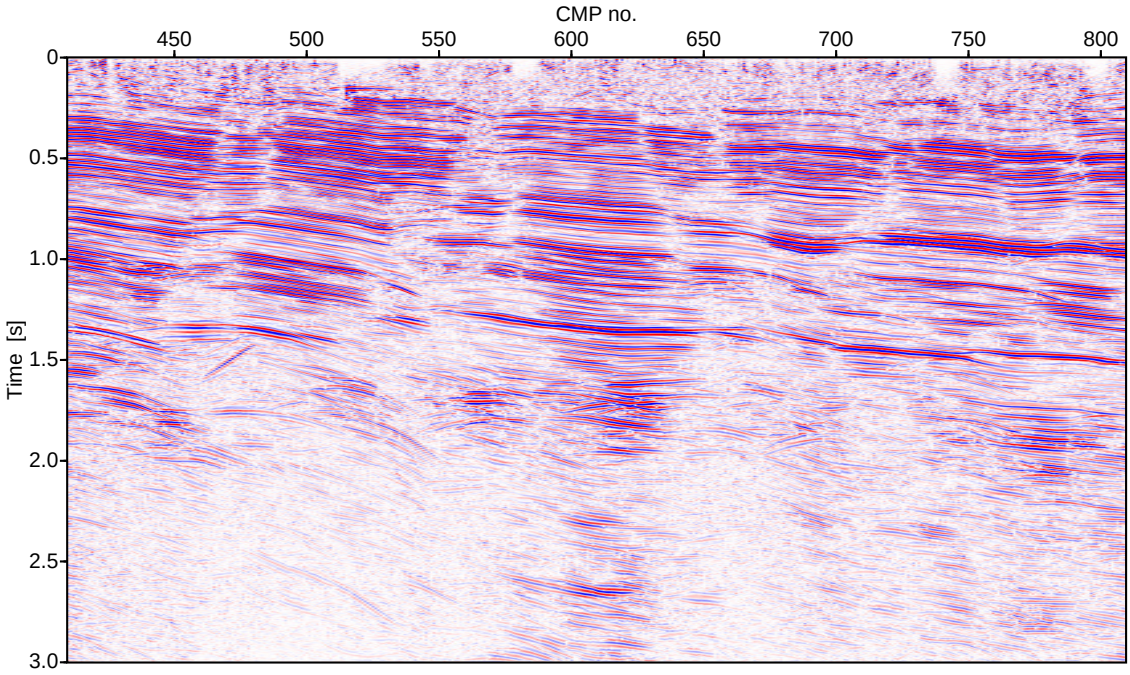

Figure 3: Result of the optimized CRS stack in the projected first Fresnel zone, Profile B.

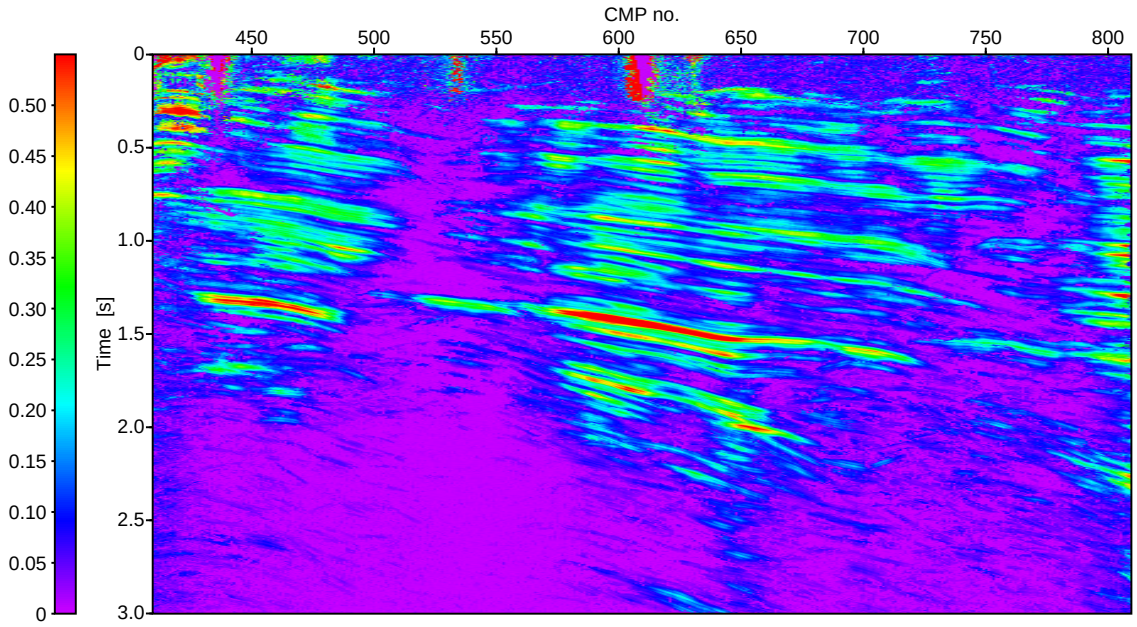

Figure 4: Coherence section associated with the CRS stack result, Profile A.

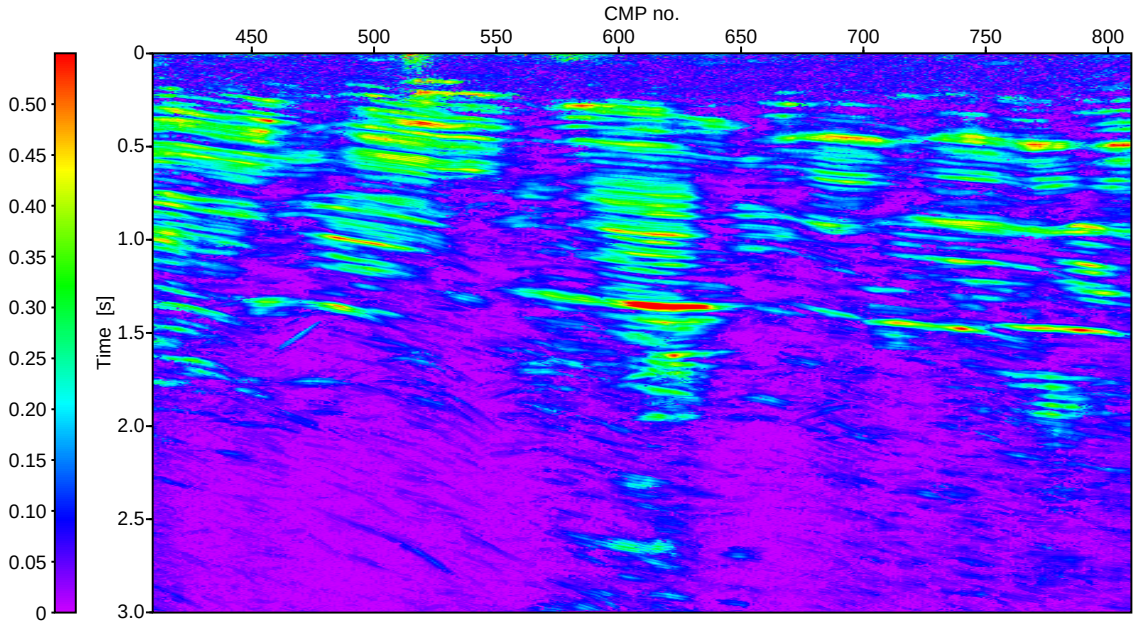

Figure 5: Coherence section associated with the CRS stack result, Profile B.

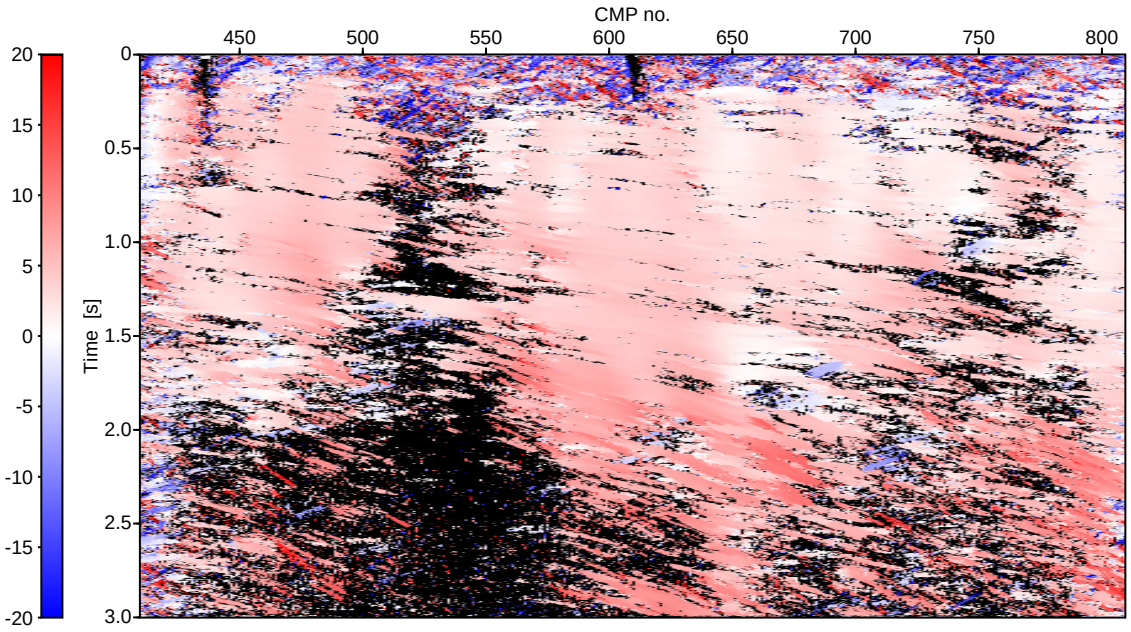

Figure 6: Emergence angle [°] of the ZO ray, Profile A. ZO samples with very low coherence value are masked out (black), as they are not expected to be related to reliable attributes.

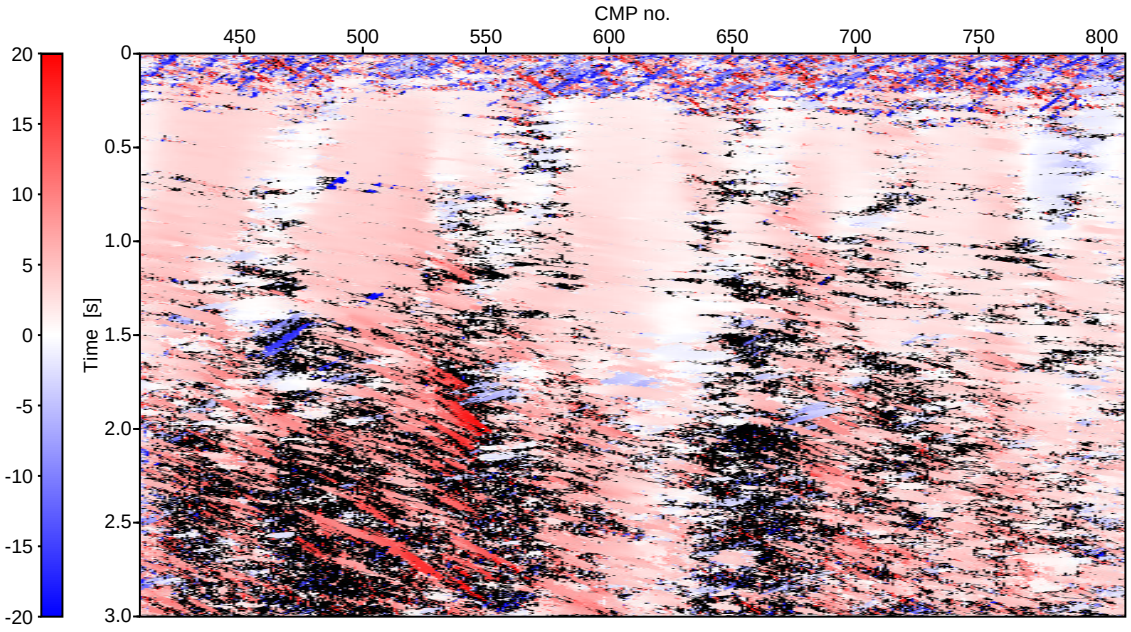

Figure 7: Emergence angle [°] of the ZO ray, Profile B. ZO samples with very low coherence value are masked out (black), as they are not expected to be related to reliable attributes.

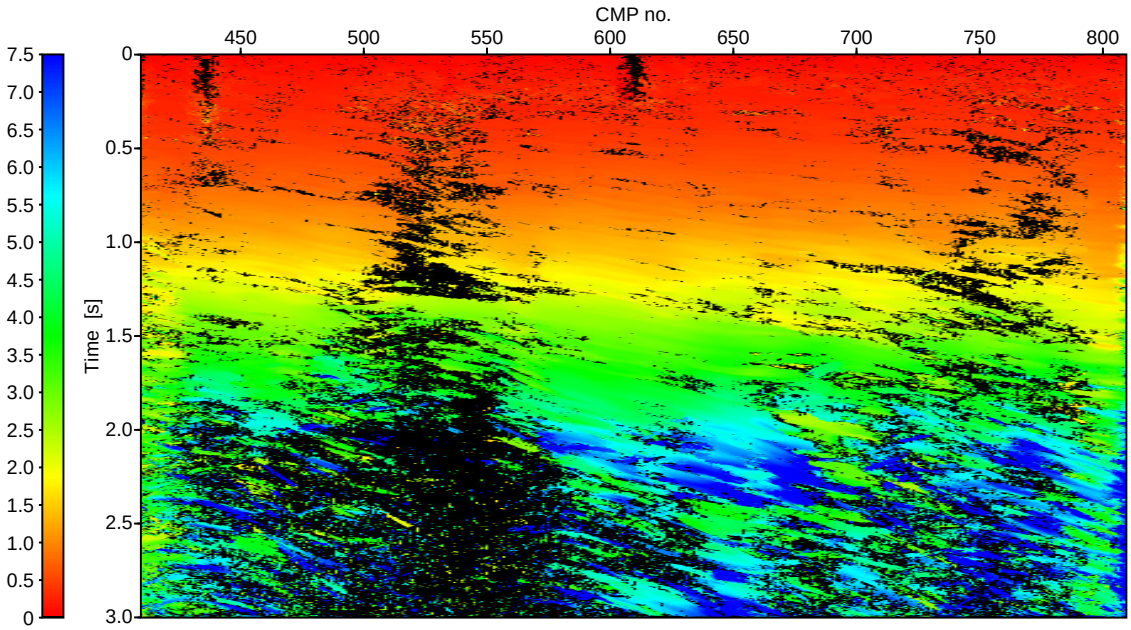

Figure 8: Radius of curvature of the NIP wavefront [km], Profile A. ZO samples with very low coherence value are masked out (black), as they are not expected to be related to reliable attributes.

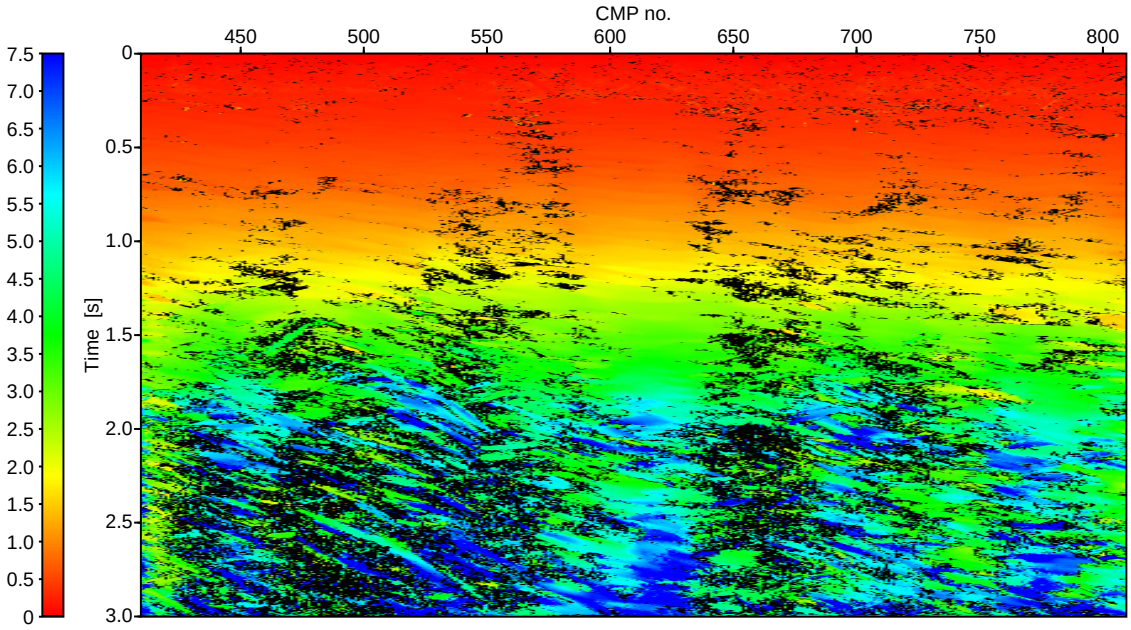

Figure 9: Radius of curvature of the NIP wavefront [km], Profile B. ZO samples with very low coherence value are masked out (black), as they are not expected to be related to reliable attributes.

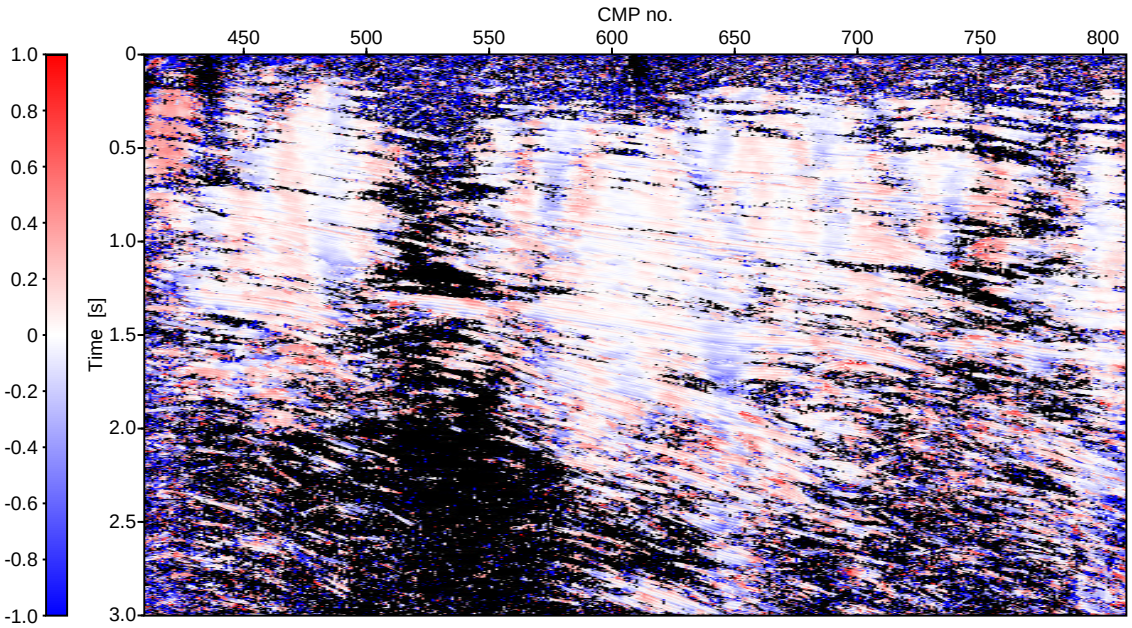

Figure 10: Curvature of the normal wave [1/km], Profile A. ZO samples with very low coherence value are masked out (black), as they are not expected to be related to reliable attributes.

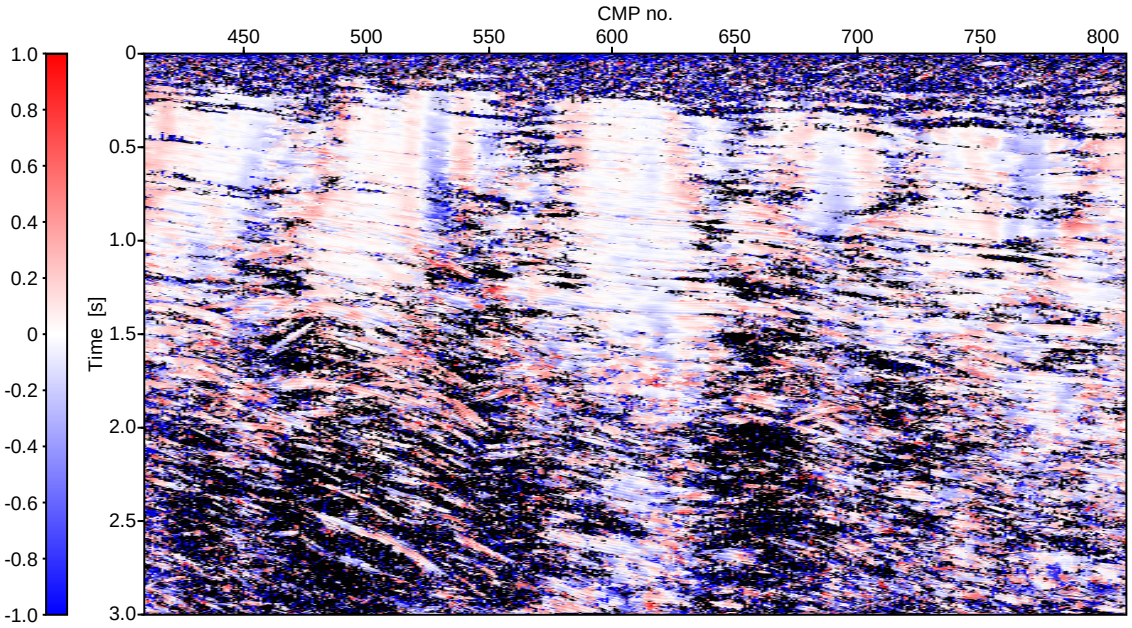

Figure 11: Curvature of the normal wave [1/km], Profile B. ZO samples with very low coherence value are masked out (black), as they are not expected to be related to reliable attributes.

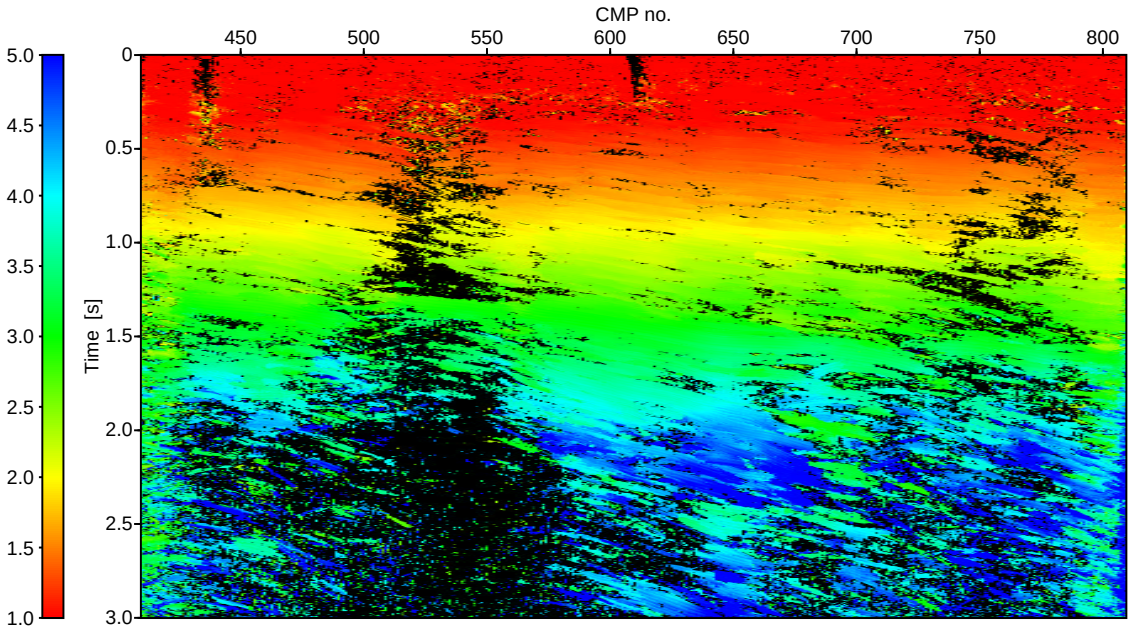

Figure 12: Optimized stacking velocity [km/s] calculated from CRS attributes, Profile A. ZO samples with very low coherence value are masked out (black), as they are not expected to be related to reliable attributes.

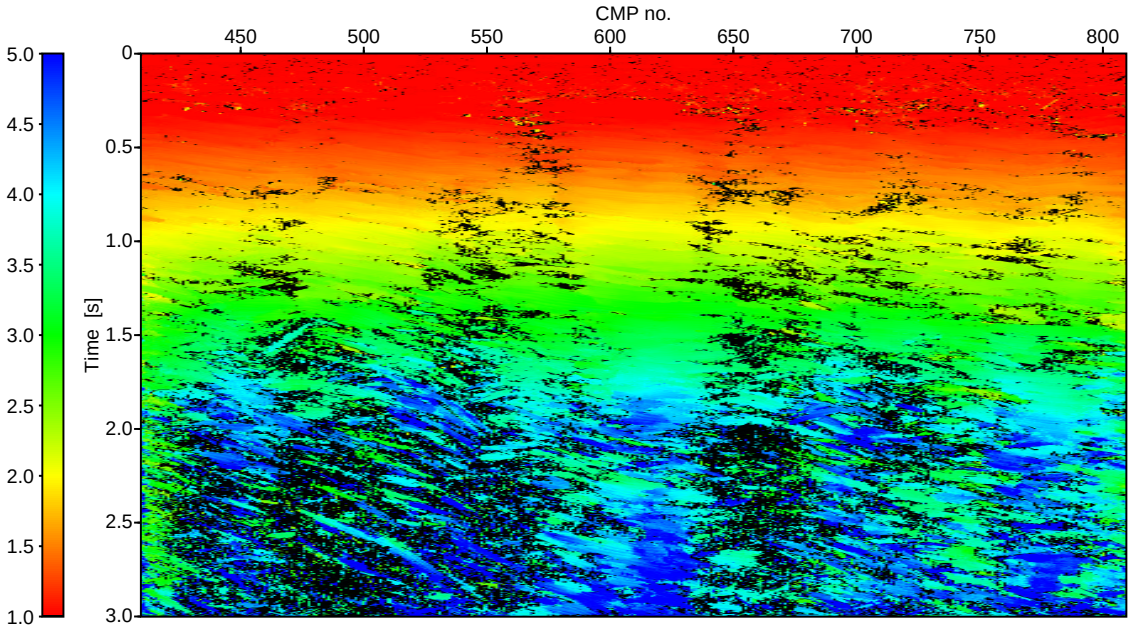

Figure 13: Optimized stacking velocity [km/s] calculated from CRS attributes, Profile B. ZO samples with very low coherence value are masked out (black), as they are not expected to be related to reliable attributes.

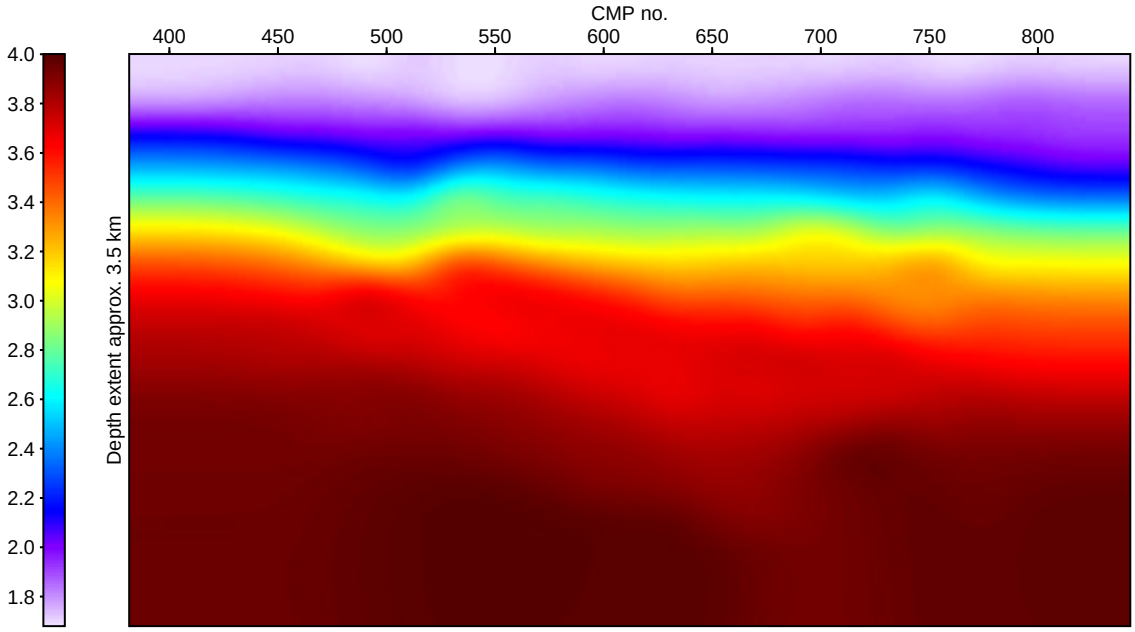

Figure 14: Macrovelocity model [km/s] obtained by CRS-attribute-based tomography, Profile A.

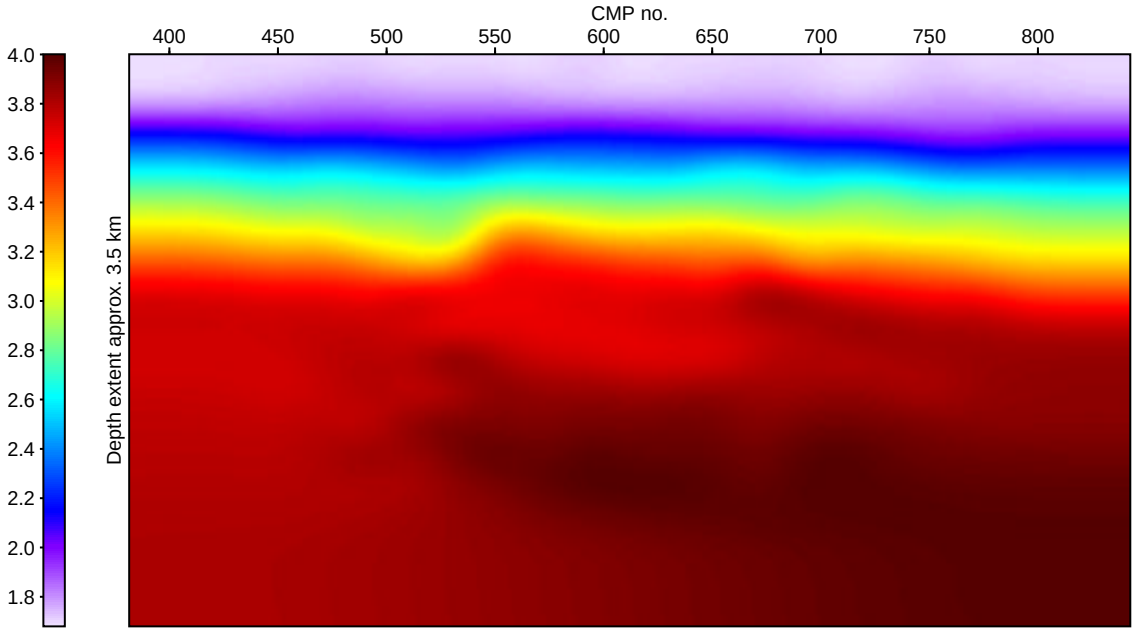

Figure 15: Macrovelocity model [km/s] obtained by CRS-attribute-based tomography, Profile B.

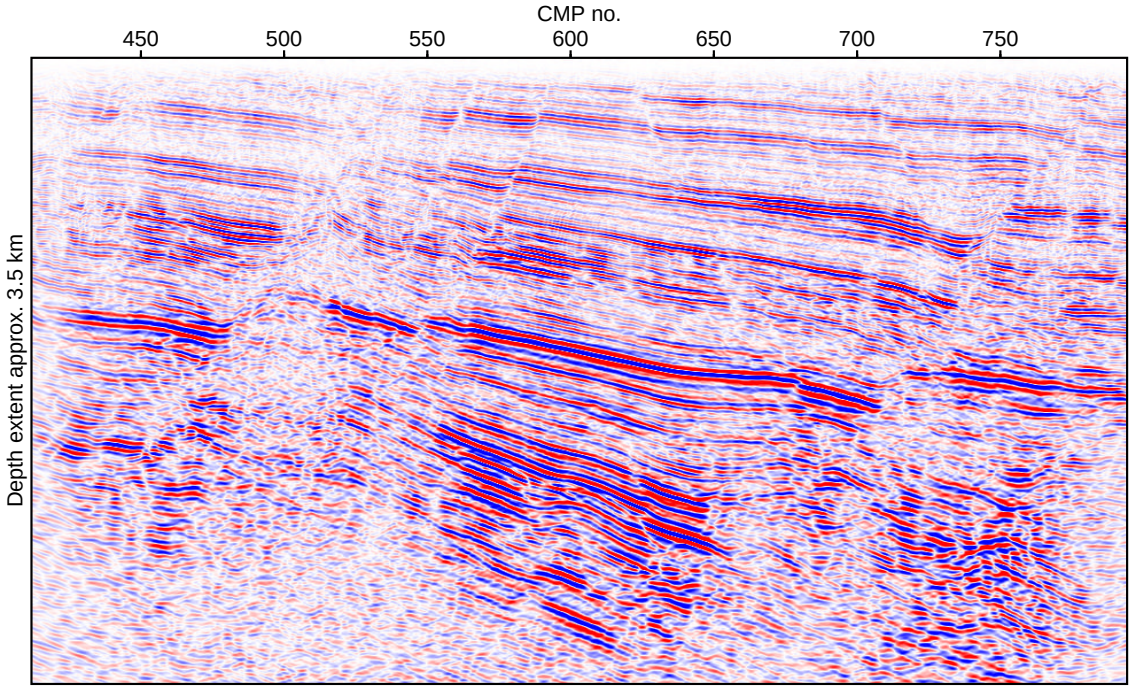

Figure 16: Prestack depth migration result, Profile A.

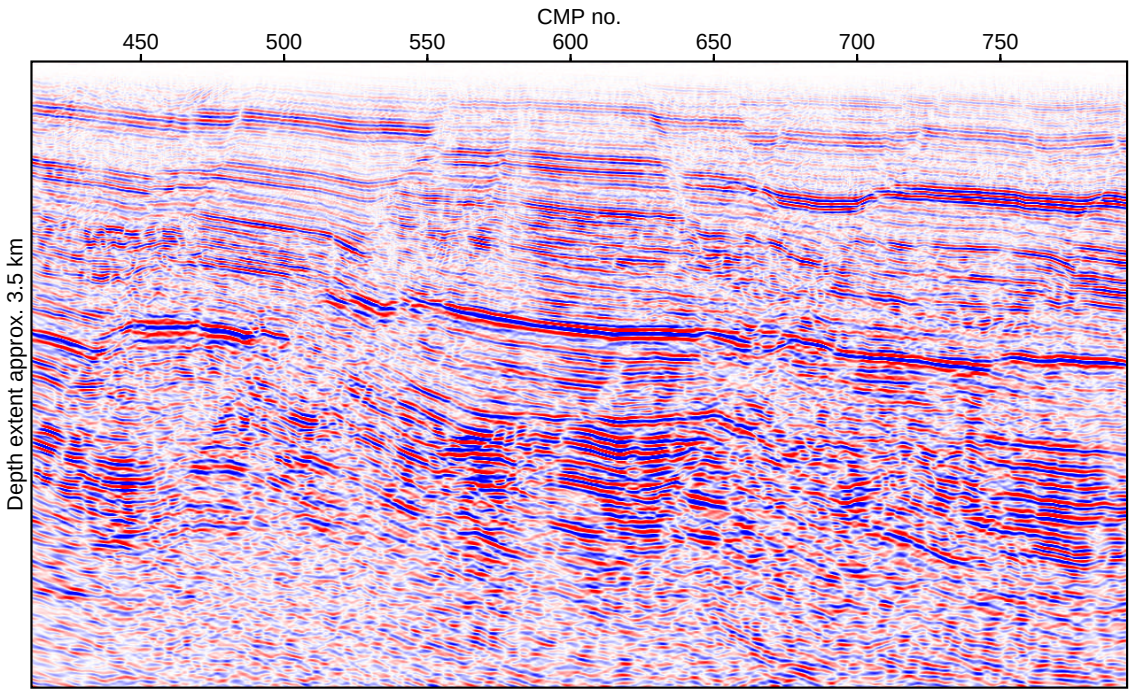

Figure 17: Prestack depth migration result, Profile B.

Poststack depth migration

As a complementary or alternative step of the CRS-stack-based imaging workflow, a poststack depth migration for both profiles was performed. Input for the poststack depth migration are the CRS-stacked sections and the macrovelocity models derived from the CRS attributes. Due to the fact that, unlike as for prestack migration, only one section is migrated to depth, the computational costs of poststack migration are much lower. In addition, poststack depth migration can be advantageous in cases where the determination of a sufficiently accurate macrovelocity model is difficult and/or the signal-to-noise ratio is poor. However, in the case discussed here, where the data quality is very high and the obtained macrovelocity models are reliable, poststack depth migration cannot compete against prestack depth migration in view of resolution and image quality, as can be seen in Figures 18 and 19. In particular, the faults and fractures are not as well resolved as by the prestack depth migration and the shallow area down to 750 m depth is slightly worse imaged. Nevertheless, there are also regions, especially at greater depths, where some details are better resolved than by the prestack depth migration. Thus, the poststack depth-migrated results can provide complementary information in crucial questions of geological interpretation even in this case.

CONCLUSIONS

The research collaboration presented in this paper is an ongoing project. Currently, the geological interpretation of the depth migration results is in progress. Presumably, an AVO analysis will follow before the drilling of the first borehole projected for early summer 2004. The high quality of the seismic data and the high transparency granted by HotRock and DMT provided an ideal basis to apply and enhance the different parts of our seismic imaging software and to demonstrate its practical applicability by means of a real data example. The obtained results provide a very good basis for the geological interpretation and for a hopefully successful drilling. The high grade of tectonic displacement of the target horizon necessary to ensure a sufficiently high production rate was verified. Due to the fact that also a standard processing sequence with up-to-date commercial software was carried out, the reliability and high quality of the results of the CRS-stack-based seismic imaging workflow could be proven.

ACKNOWLEDGMENTS

This work was kindly supported by *HotRock EWK Offenbach/Pfalz GmbH*, Karlsruhe, Germany, the *Federal Ministry for the Environment, Nature Conservation and Nuclear Safety* of Germany, and the sponsors of the *Wave Inversion Technology (WIT) Consortium*, Karlsruhe, Germany. We also like to thank *Deutsche Montan Technologie GmbH*, Essen, Germany, for good collaboration during the whole project.

REFERENCES

Duveneck, E. (2002). Tomographic velocity model inversion with CRS attributes. *Annual WIT report*, pages 92–106.

Hertweck, T. and Jäger, C. (2002). Short note: various aspects of Kirchhoff migration. *Annual WIT report*, pages 133–142.

Jäger, C. and Hertweck, T. (2002). Using Uni3D version v0.23: a manual. *Annual WIT report*, pages 143–150.

Jäger, R. (1999). The Common-Reflection-Surface stack - theory and application. Master's thesis, Karlsruhe University.

Koglin, I. and Ewig, E. (2002). Residual static corrections by means of CRS attributes. *Annual WIT report*, pages 61–70.

Mann, J. (2002). *Extensions and applications of the Common-Reflection-Surface stack method*. Logos Verlag, Berlin.

Müller, T. (1998). Common Reflection Surface Stack versus NMO/STACK and NMO/DMO/STACK. In *Extended Abstracts*. 60th Annual Internat. Mtg., Eur. Assn. Geosci. Eng. Session 1-20.

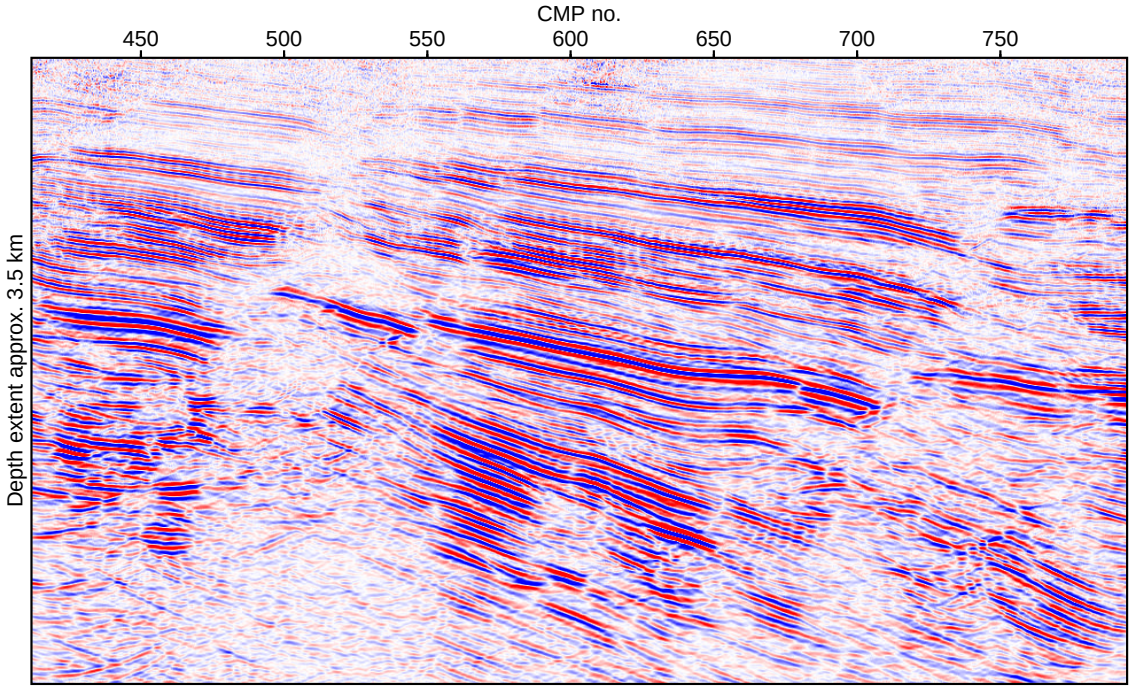

Figure 18: Poststack depth migration result, Profile A.

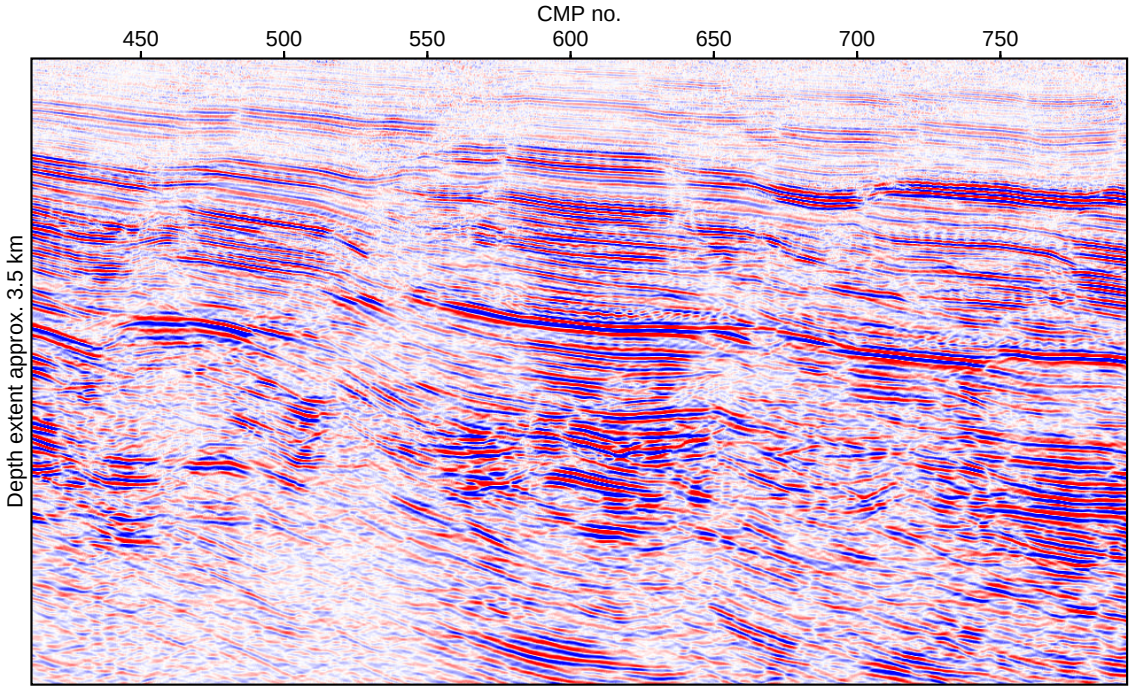

Figure 19: Poststack depth migration result, Profile B.